Effect of Harmonic Current Control of IPMSMs by Repetitive Perfect Tracking Control on Torque Ripple and Iron Loss

Yuhiro Inagaki*   Student Member,   Masahiro Mae*   Student Member

Osamu Shimizu*   Member,   Sakahisa Nagai*   Member

Hiroshi Fujimoto*   Senior Member,   Takayuki Miyajima**   Member

Yoshiki Yasuda**   Member,   Akio Yamagiwa**   Senior Member

Interior permanent magnet synchronous motors (IPMSMs) have broad applicability in the industry owing to their advantages of fast response and high torque. However, harmonic currents caused by the spatial harmonics of the magnetic flux owing to the motor structure increase iron loss and torque ripple. Suppressing harmonic currents by current control is thought to improve the drive efficiency of IPMSMs because it removes the cause of the increase in iron loss. However, this is not a control method aimed at suppressing torque ripple, including cogging torque. Many current control methods to suppress torque ripple add compensation signals to the current command, and these signals are expected to increase iron loss. In this study, we experimentally verified the effects of harmonic current suppression control and torque ripple suppression control on iron loss and torque ripple, and confirmed the trade-off relationship. The current controller in the experiment is based on repetitive perfect tracking control (RPTC).

Keywords: IPMSM, iron loss, harmonic current suppression, torque ripple suppression, repetitive perfect tracking control

1. Introduction

Permanent Magnet Synchronous Motors (PMSMs) have a wide range of applications in the industry because of their high torque and fast control response. Among PMSMs, IPMSMs can obtain higher torque because they can utilize reluctance torque. However, harmonic current owing to spatial harmonics of the magnetic flux caused by the motor structure cause degradation of various characteristics. For example, the harmonic current increases the copper loss caused by the resistance of the windings and the iron loss caused in the electromagnetic steel sheet, decreasing the operating efficiency. In addition, the harmonic current also increases torque ripple, which causes vibration and noise in the equipment.

Many current controllers to improve the efficiency considering harmonic current have been proposed. However, some methods do not consider iron loss [1], and even those that consider the iron loss have problems with the accuracy of the iron loss model [2][3]. Since the iron loss is difficult to measure directly, modeling is problematic, and there are many issues to be considered, such as simplifying the model into a form that is easy to handle in the control system while maintaining accuracy, and the existence of parameters that are difficult to measure in advance.

Many torque ripple suppression controllers use a compensation signal for torque ripple added to the current command [4][5]. However, the compensation signal added in this way is thought to have the same problem of increasing iron loss as in the case of harmonic currents.

To solve the problems of harmonic current and torque ripple, our research group has proposed repetitive perfect tracking control (RPTC) [6][7] that focuses on their periodicity synchronized with the rotation. RPTC is based on perfect tracking control (PTC) [8].

In this paper, a current controller that can change the degree of harmonic current suppression and torque ripple suppression is implemented using RPTC. The effects of harmonic current suppression control and torque ripple suppression control on iron loss and torque ripple were verified by this current controller. By suppressing the harmonic current through RPTC, the cause of iron loss increase can be removed, and iron loss can be reduced without using a complicated iron loss model. In addition, since the degree of torque ripple suppression can be changed with simple parameters, system users can adjust the degree of efficiency improvement and torque ripple suppression according to their requirements.

2. Modeling of IPMSM and Characteristics of Iron Loss and Torque Ripple

2.1 Plant Model of the IPMSM   The IPMSM model on the dq-axis system is shown in Fig. 1. In this study, current controllers were designed on the dq-axis. The different parameters are listed in Table 1. The dq-axis voltage equation is expressed as follows:

$$\begin{bmatrix} v_d \\ v_q \end{bmatrix} = \begin{bmatrix} R + sL_d & -\omega_e L_q \\ \omega_e L_d & R + sL_q \end{bmatrix} \begin{bmatrix} i_d \\ i_q \end{bmatrix} + \begin{bmatrix} 0 \\ \omega_e K_e \end{bmatrix} .(1)$$

In general, the dq-axis voltage is decoupled as follows:

$$v_d = v'_d - \omega_e L_q i_q, \cdots\cdots\cdots\cdots\cdots\cdots\cdots\cdots\cdots(2)$$

* The University of Tokyo
  5-1-5, Kashiwanoha, Kashiwa, Chiba, 277-8561, Japan
** DAIKIN INDUSTRIES, Ltd.
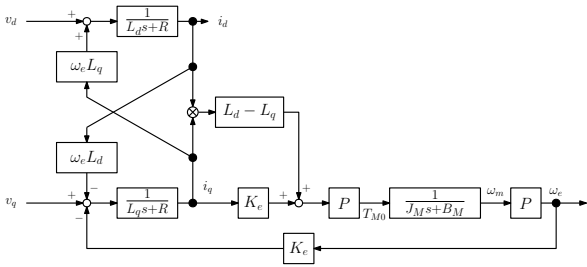 1-1-1, Nishi-Hitotsuya, Settsu, Osaka 566-8585, Japan

Fig. 1.　Block diagram of the IPMSM model.

Table 1.　Parameters of the IPMSM and their interpretation.

Parameter	Meaning
v_d, v_q	dq-axis voltage
i_d, i_q	dq-axis current
L_d, L_q	dq-axis inductance
R	Resistance of windings
K_e	Permanent-magnet flux linkage
P	Number of pole pairs
J_M	Motor inertia
B_M	Viscous friction coefficient
ω_m	Mechanical angular velocity
ω_e	Electric angular velocity

$$v_q = v_q' + \omega_e(L_d i_d + K_e). \quad\cdots\cdots\cdots\cdots\cdots\cdots\cdots\cdots (3)$$

When the state variable is defined as the dq-axis current and the input as the decoupled dq-axis voltage, the continuous-time state and output equations of the IPMSM are expressed as follows:

$$\dot{\boldsymbol{x}}(t) = A_c \boldsymbol{x}(t) + B_c \boldsymbol{u}(t), \quad\cdots\cdots\cdots\cdots\cdots\cdots\cdots (4)$$

$$\boldsymbol{y}(t) = C_c \boldsymbol{x}(t) + D_c \boldsymbol{u}(t), \quad\cdots\cdots\cdots\cdots\cdots\cdots\cdots (5)$$

where

$$\boldsymbol{x}(t) = \left[\begin{array}{c} i_d(t) \\ i_q(t) \end{array}\right], \boldsymbol{u}(t) = \left[\begin{array}{c} v_d'(t) \\ v_q'(t) \end{array}\right], \quad\cdots\cdots\cdots\cdots\cdots (6)$$

$$\left\{ \begin{array}{l} A_c = \left[\begin{array}{cc} -\frac{R}{L_d} & 0 \\ 0 & -\frac{R}{L_q} \end{array}\right], B_c = \left[\begin{array}{cc} \frac{1}{L_d} & 0 \\ 0 & \frac{1}{L_q} \end{array}\right], \\ C_c = \left[\begin{array}{cc} 1 & 0 \\ 0 & 1 \end{array}\right], D_c = O. \end{array}\right. \quad\cdots (7)$$

2.2　Harmonic Components in General Iron Loss Model　Many efficiency improvement control methods considering iron loss use iron loss models based on Steinmetz iron loss formula or Bertotti iron loss formula [3][9]. As an example, the basic form of Bertotti's equation is shown as follows [10]:

$$\rho_{ir} \simeq C_0 B_{max}^2 f_m + \frac{\pi^2 \sigma d^2}{6\delta}(B_{max} f_m)^2 + C_1(B_{max} f_m)^{1.5}, (8)$$

where ρ_{ir} is the iron loss per unit mass, C_0 and C_1 are parameters determined by material properties, σ is the electrical conductivity, d is the thickness of the lamination, δ is the density of the material, B_{max} is the maximum magnetic flux density, and f_m is the magnetization frequency. From this model, it can be seen that the magnetic flux density of the higher frequency components increases the iron loss.

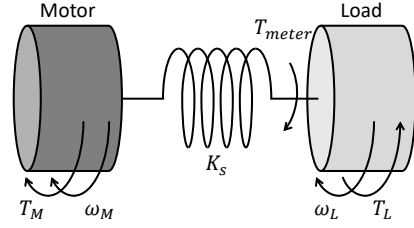In addition, when calculating the iron loss owing to harmonics, an approximate calculation is sometimes used. Iron loss is calculated for each harmonics order, and the sum of these is used as the iron loss as follows [11]~[13]:

$$P_{ir} = \sum_n P_{ir,n}, \quad\cdots\cdots\cdots\cdots\cdots\cdots\cdots\cdots\cdots\cdots\cdots (9)$$

where n is harmonics order and P_{ir} is the iron loss. From Eq. (9), it is expected that suppressing the harmonic current and reducing the harmonic components of the magnetic flux density reduces the iron loss.

2.3　Torque Ripple Measurement　Various efforts have been made in the measurement method in the study of torque ripple suppression. Torque meters, which are often used for torque measurement, measure the motor torque by multiplying the shaft torsion angle caused by the torque of the driving side and load side motors by the spring coefficient. In this study, the torque ripple is estimated by assuming that the system consisting of motors and a torque meter is a two-inertia system. The schematic diagram and block diagram of a typical two-inertia system are shown in Fig. 2 and Fig. 3.

To control and evaluate the torque ripple, it is necessary to estimate the torque T_M in Fig. 3 and obtain its frequency component. Using encoder position data θ_M and measured value of the torque meter T_{meter}, motor torque T_M is estimated as follows [14]:

$$T_M = T_{meter} + T_{ev} = T_{meter} + J_M \ddot{\theta}_M + B_M \dot{\theta}_M. \quad\cdots\cdots (10)$$

In this research, the central difference was used to calculate the angular velocity and angular acceleration, assuming that the RPTC can use the one sample ahead data because it records the encoder position information in memory.

3.　Design of Current Controller

3.1　Design of the feedback controller　In general, the PI controller is used for current control. A typical current feedback control system is shown in Fig. 4. The PI controller

Fig. 2.　Schematic diagram of the two-inertia system.

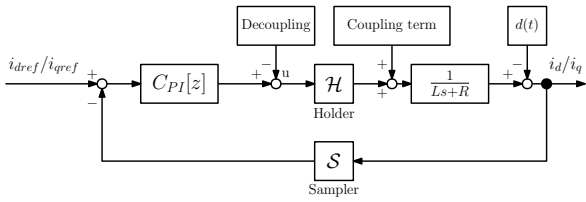Fig. 3.　Block diagram of the two-inertia system.

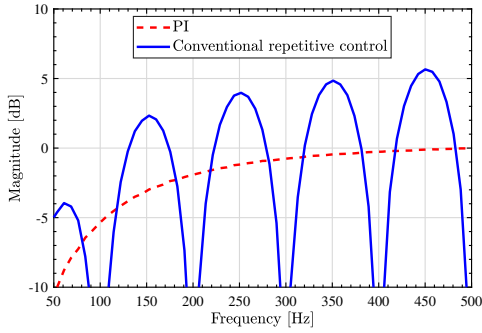Fig. 4. General current PI controller.

Fig. 5. Sensitivity function of the PI controller and the repetitive control based on the internal model principle.
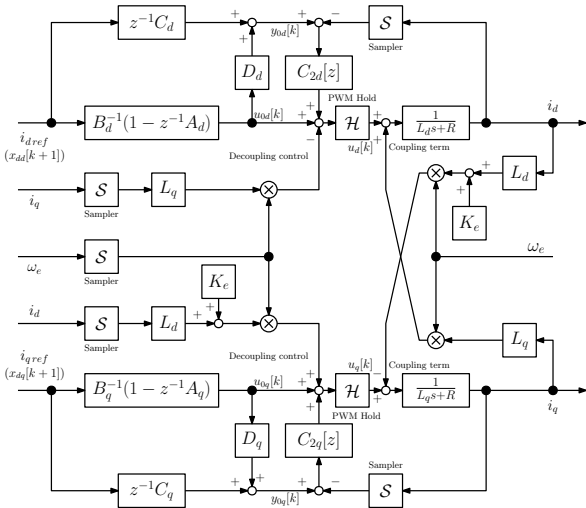

Fig. 6. Block diagram of the PTC (*dq*-axis current).

$C_{PI}(s)$ designed by pole-zero cancellation is as follows:

$$C_{PI}(s) = \frac{Ls + R}{\tau s}. \cdots\cdots\cdots\cdots\cdots\cdots\cdots\cdots\cdots (11)$$

τ is often set to approximately 10 times the control period. $C_{PI}[z]$ is the discretized $C_{PI}(s)$. From Eq. (4) and Eq. (5), the transfer function from the current command $i_{d,q\,ref}$ to the actual current $i_{d,q}$ is as follows:

$$\frac{i_{d,q}}{i_{d,q\,ref}} = \frac{1}{\tau s + 1}. \cdots\cdots\cdots\cdots\cdots\cdots\cdots\cdots (12)$$

Fig. 5 shows the sensitivity function from the output end disturbance ($d(t)$ in Fig. 4) to the output. This figure shows the sensitivity functions of PI controller and repetitive control based on the internal model principle. It can be seen that it is difficult to suppress the harmonic current and extend the control bandwidth with PI control.

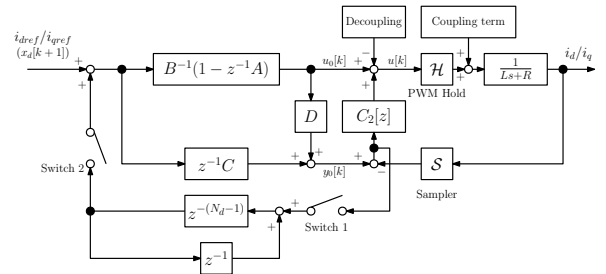**3.2 PTC** [8]   The block diagram of the PTC on the *dq*-

Fig. 7. Block diagram of RPTC with switches.

axis is shown in Fig. 6. Subscripts *d* and *q* indicate that each coefficient and variable are calculated on its axis. The control system by PTC has a stable inverse system as feed-forward controller and PI controller ($C_2[z]$) as feedback controller. In the *n* th-order plant model, it is necessary to switch the control input *n* times. However, the *dq*-axis plant model of IPMSM shown in Fig. 6 is a first-order model, and single-rate implementation is sufficient.

To design the feed-forward controller of PTC, the state equation (Eq. (4)) and the output equation of (Eq. (5)) are discretized by the PWM hold [15]. PWM hold is the strict hold method based on the pulse voltage composed of the inverter supply voltage $\pm E\,[\text{V}]$ and $0\,[\text{V}]$, instead of assuming that the inverter can output an arbitrary voltage. The control input $u[k]$ is the inverter ON time, and PWM hold is more suitable than the zero-order hold for instantaneous value control [16][17]. The discrete time state and output equation of the IPMSM based on the PWM hold are expressed as follows:

$$x[k + 1] = Ax[k] + Bu[k], \cdots\cdots\cdots\cdots\cdots\cdots (13)$$
$$y[k] = Cx[k] + Du[k]. \cdots\cdots\cdots\cdots\cdots\cdots (14)$$

A, B, C, and D are calculated using Eq. (15). T_u is the control input period. E is the DC power supply voltage of a 3-phase inverter.

$$A = e^{A_c T_u}, \; B = e^{A_c T_u/2} B_c E, \; C = C_c, \; D = D_c. \cdots (15)$$

From Eq. (13), and Eq. (14), the stable inverse model, and the nominal output of PTC are expressed as Eq. (16), and Eq. (17).

$$u_0[k] = B^{-1}(1 - z^{-1}A)x_d[k + 1], \cdots\cdots\cdots\cdots (16)$$
$$y_0[k] = z^{-1}Cx_d[k + 1] + Du_0[k]. \cdots\cdots\cdots\cdots (17)$$

The inverse system of PTC improves the tracking characteristic to the command value, and the tracking errors owing to modeling errors and external disturbances are suppressed by the feedback control of the PI controller ($C_2[z]$).

3.3 RPTC [6]

3.3.1 Harmonic Current Suppression RPTC (HCS RPTC) [7]   This section describes HCS RPTC which suppresses the harmonic currents. The block diagram of HCS RPTC is shown in Fig. 7. The decoupling control and coupling terms are the same as those in Fig. 6. The RPTC system has a periodic signal generator (PSG). The PSG records the tracking error caused by the harmonic current as the periodic error in the memory and uses it for compensation. The internal structure of the PSG is shown in detail in Fig. 8.

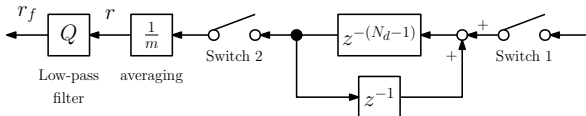As shown in the block diagram in Fig. 7 and Fig. 8, HCS
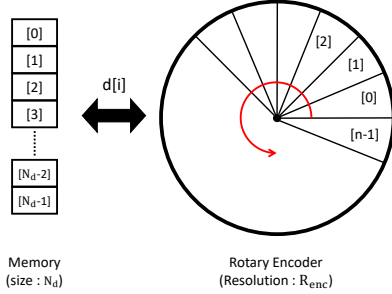
Fig. 8.   Block diagram of the PSG.

Fig. 9.   PSG for handling speed variations.

RPTC is equipped with two switches. At first, only switch 1 is turned ON to start recording the error, and when the recording is complete, switch 1 is turned OFF and switch 2 is turned ON. By turning on switch 2, RPTC can suppress the harmonic current like feed-forward control. In contrast to repetitive controllers based on the internal model principle, the feed-forward-like compensation signal of RPTC has the advantage of not exacerbating the inter-order harmonics.

To design the PSG, we explain the memory settings at first. The memory size is defined as N_d, and expressed by Eq. (18) using the cyclical tracking error period T_d and the control period T_s.

$$N_d = \frac{T_d}{T_s}. \cdots\cdots\cdots\cdots\cdots\cdots\cdots\cdots\cdots\cdots\cdots\cdots (18)$$

In addition, to remove asynchronous components and noise from the compensation signal, the errors of m periods are recorded and averaged, then passed through a low-pass filter Q before the compensation signal is added to the current command. The low-pass filter Q takes the following form to avoid the phase delay [18].

$$r_f[k] = Qr[k] = \frac{z + \gamma + z^{-1}}{\gamma + 2} r[k], \cdots\cdots\cdots\cdots (19)$$

where $r_f[k]$ is the filter output, $r[k]$ is the PSG output, and γ is the design parameter of the filter.

Assuming that the harmonic current is influenced by the spatial harmonics of the magnetic flux, the appearance of the compensation signal is considered to be highly dependent on the rotor position. Using this characteristic, RPTC links the memory and the encoder position data as shown in Fig. 9. This makes it possible to handle speed variation [19].

3.3.2   Torque Ripple Suppression RPTC (TRS RPTC) [14]

In this section, Torque Ripple Suppression RPTC of IPMSM is described. The block diagram of TRS RPTC is shown in Fig. 10. Assuming that the magnet torque is sufficiently larger than the reluctance torque, this block diagram controller is applied to the q-axis current. On the d-axis current, HCS RPTC is used to suppress the harmonic current continuously. This controller has four switches on the q-axis.
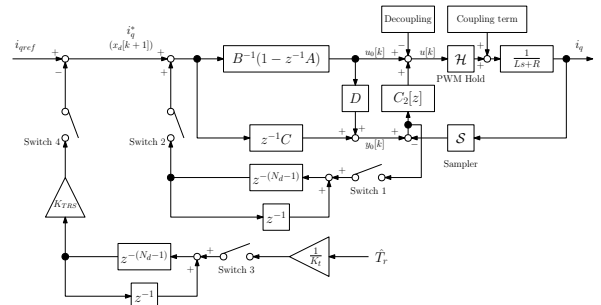

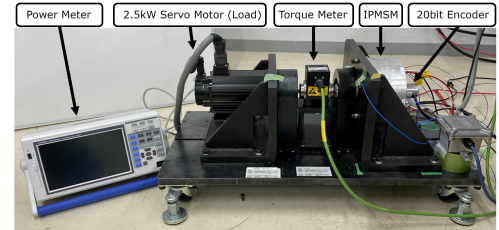Fig. 10.   Block diagram of TRS RPTC (Proposed method).

Fig. 11.   Experimental setup.

The operation procedures of these switches and the operation flow of the TRS RPTC are shown as follows.

(1)   At first, all switches are left OFF, and tracking to the current command is started.

(2)   Turn on the switch 1 ON both dq-axis and start recording the current tracking errors.

(3)   After recording is completed for m cycles, the switch 1 is turned OFF and the switch 2 is turned ON. This operation starts the harmonic suppression on each dq-axis through the low-pass filter Q.

(4)   After reaching the steady-state, turn ON the switch 3 on the q-axis to start recording the position data of encoder. No new operation is applied to the d-axis, and the d-axis harmonic current suppression is continued.

(5)   The position data of encoder is recorded in the memory for p periods and averaged. The torque ripple T_r is estimated from that data and the measured value of the torque meter. The estimated data is divided by the torque coefficient K_t and converted into the compensation signal to be given to the current command.

(6)   After the compensation signal is generated, the switch 3 is turned OFF and the switch 4 is turned ON. The compensation signal is added to the current command through the low-pass filter Q and a parameter K_{TRS} ($0 \leqq K_{TRS} \leqq 1$) set by users.

The torque ripple is estimated from the angular velocity and angular acceleration calculated from the encoder, the inertia and friction coefficient obtained from the system identification, and the torque meter measurement value as shown in Eq. (10). This estimated value also includes the cogging torque.

The torque constant K_t is obtained as follows, taking the reluctance torque into account:

$$K_t = P\{K_e + (L_d - L_q)I_d\}. \cdots\cdots\cdots\cdots\cdots\cdots (20)$$

To extract only the ripple component $\hat{T}_r$ from the estimated

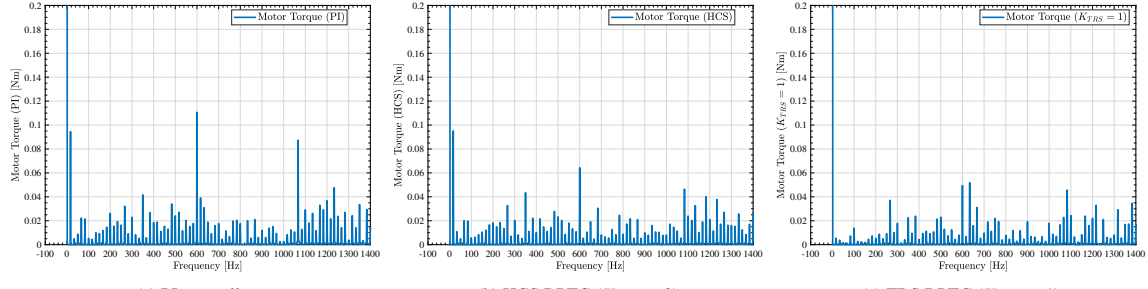(a) PI controller (b) HCS RPTC ($K_{TRS} = 0$) (c) TRS RPTC ($K_{TRS} = 1$)

Fig. 12. Magnified view of the motor torque DFT results focusing on the 6th order component.

Table 2. Parameters of the experimental IPMSM and experimental condition.

Parameter	Value
d-axis inductance L_d	0.613 mH
q-axis inductance L_q	1.21 mH
Resistance R	85.6 mΩ
Permanent magnet flux linkage K_e	31.2 mWb
Pole pairs P	6
Supply voltage V_{dc} (E)	100 V
Carrier frequency F_s	10 kHz
Control period T_s	0.1 ms
Motor inertia J_M	3.11×10^{-3} kgm^2
Viscous friction coefficient B_M	3.21×10^{-4} Nm · s/rad

torque, the zero-order component is removed by subtracting the average of one period of the memory from the estimated torque when it is used as the compensation signal.

4. Experiment Using Motor Bench

4.1 Experimental Setup   Fig. 11 shows the motor bench used in the experiment. The power meter PW3390 (HIOKI) can measure in units of 0.01 W, and the torque meter TMB307/411 (MAGTROL) can measure up to 10 Nm with an accuracy of ±0.15%. The bandwidth of this torque meter is 5 kHz. The parameters of IPMSM and experimental conditions are listed in Table 2. The rotation speed condition was set to 1000 rpm (electric angular frequency:100 Hz), and the q-axis current command given to the IPMSM was set to 10 A, and the d-axis current command was set to −1.86 A based on the MTPA conditional formula [20].

$$i_{d\,ref} = \frac{K_e}{2(L_q - L_d)} - \sqrt{\frac{K_e^2}{4(L_q - L_d)^2} + i_{q\,ref}^2} \cdots \cdots (21)$$

All memory sizes N_d used in RPTC were determined to be 600 with the basic period to be suppressed set to the rotation frequency. The average number of current errors m was 10 and the average number of position data for torque ripple measurement p is 150. The torque ripple measurement also averaged the encoder position data 150 times. The parameter γ of low-pass filter Q was set to 2, and the cutoff frequency was 1.8 kHz. The parameter τ of PI controller was set to $10T_s = 1$ ms. Tustin transformation was used for discretization, and the transformation period was T_s.

The iron loss was measured by subtracting the output and other losses from the input power to the IPMSM as follows:

$$P_{ir} = P_{in} - P_{out} - P_{co} - P_{me}, \cdots \cdots \cdots \cdots (22)$$

$$P_{out} = T_{meter}\omega_m, \cdots \cdots \cdots \cdots \cdots \cdots \cdots (23)$$

Table 3. Experimental temperature and phase resistance.

Parameter	Value
Initial winding temperature T_{STi}	20.3 °C
U phase resistance $R_u(T_{STi})$	86.3 mΩ
V phase resistance $R_v(T_{STi})$	88.1 mΩ
W phase resistance $R_w(T_{STi})$	86.7 mΩ
Temperature coefficient α	3.92×10^{-3}

$$P_{co} = I_{u\,rms}^2 R_u + I_{v\,rms}^2 R_v + I_{w\,rms}^2 R_w, \cdots \cdots \cdots \cdots (24)$$

where P_{in} is the input power, P_{out} is the output power, P_{co} is the copper loss, P_{ir} is the iron loss, and P_{me} is the mechanical loss. $I_{u\,rms}$, $I_{v\,rms}$ and $I_{w\,rms}$ are the phase currents. R_u, R_v and R_w are the resistances of the windings. The winding resistance used in the copper loss calculation is temperature corrected as follows [21]:

$$R(T_{ST}) = R(T_{STi})\{1 + \alpha(T_{ST} - T_{STi})\}, \cdots \cdots \cdots (25)$$

where T_{ST} is the winding temperature, T_{STi} is the initial winding temperature and α is the temperature coefficient of the copper resistance (20.3 °C). The parameters related to resistance are as shown in Table 3.

4.2 Experimental Result   The iron loss and the torque ripple of pole-zero cancellation PI controller, HCS RPTC ($K_{TRS} = 0$) and TRS RPTC were measured. All measurements are averaged over 1 second, and the average of 10 times for each controller is used. The relationship between the degree of torque ripple suppression and the iron and total loss was investigated by changing the coefficient K_{TRS}, which adjusts the magnitude of the compensation signal, to 0, 0.25, 0.5, 0.75, and 1.

At first, the discrete Fourier transform (DFT) results of torque are shown in Fig. 12, which are magnified graphs focusing on the 6th order torque ripple. Furthermore, the ratio of the 6th order torque ripple to the average torque measured by the torque meter are shown in Fig. 13. The results in Fig. 13 are the average of 10 times for each case (PI, HCS, $K_{TRS} = 0.25, 0.5, 0.75, 1$), and the results in Fig. 12 are representative examples. Fig. 14 shows the ratio of iron loss and total loss to the input power. TRS suppresses all integer multiple components of the PSG memory period. However, we focus on the 6th order component, which is particularly significant.

Fig. 13 shows that 18 % of the torque ripple amplitude caused in the case of HCS RPTC was reduced in the case of $K_{TRS} = 1$. As for the iron loss, it was confirmed that 0.2 % of the iron loss caused by PI control was reduced by HCS RPTC. In addition, Fig. 14 shows that the iron loss in HCS
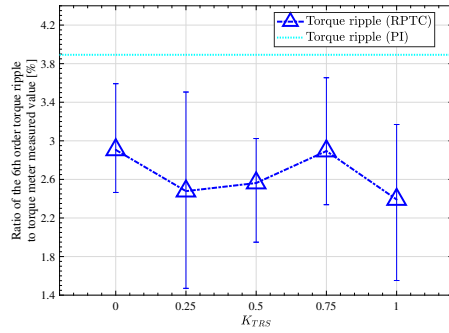
Fig. 13. Ratio of the 6th order torque ripple to average torque for each torque ripple compensation signal coefficient K_{TRS}.
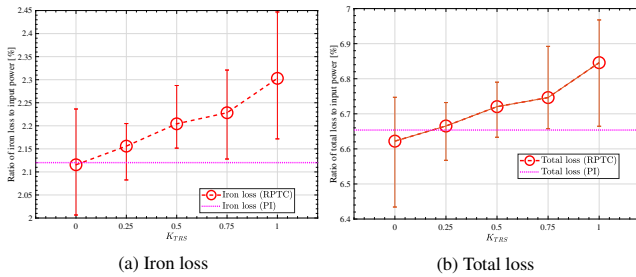

(a) Iron loss   (b) Total loss

Fig. 14. Ratio of iron and total loss to average input power for each torque ripple compensation signal coefficient K_{TRS}.

RPTC was increased by 8.9 % in K_{TRS} = 1 case. The efficiency in HCS RPTC was 93.4 %, while that in $K_{TRS=1}$ case was 93.2 %.

As the coefficient K_{TRS} multiplied by the torque ripple compensation signal was increased, the iron loss increased, and the efficiency decreased. In addition, the torque ripple tended to be generally reduced. However, the case of K_{TRS} = 0.75 deviated from the tendency. It is assumed that this is because the compensation signal caused the modeling error on both the *dq*-axes owing to the coupling term that could not be completely decoupled.

5. Conclusion

In this paper, we focused on the harmonic current of IPMSMs and confirmed the trade-off relationship between the iron loss and the torque ripple when the harmonic current was suppressed by HCS RPTC and when the torque ripple was suppressed by TRS RPTC. Users of this system can easily adjust the balance by looking at these torque ripple and loss characteristics.

References

(1) J. Qu, J. Jatskevich, C. Zhang, and S. Zhang, "Torque Ripple Reduction Method for Permanent Magnet Synchronous Machine Drives with Novel Harmonic Current Control," *IEEE Transactions on Energy Conversion*, vol. 8969, no. c, pp. 1–11, 2021.

(2) H. Zhang, M. Dou, and C. Dang, "Loss-Optimization Method of Permanent-Magnet Synchronous Motor Based on Precise Stator Iron Loss Model," *IEEE Journal of Emerging and Selected Topics in Power Electronics*, vol. 9, no. 5, pp. 5407–5415, 2020.

(3) Q. Guo, C. Zhang, L. Li, J. Zhang, and M. Wang, "Maximum efficiency per torque control of permanent-magnet synchronous machines," *IEEE Transactions on Industrial Electronics*, vol. 62, no. 4, pp. 2135–2143, 2015.

(4) K. Yoshimoto and Y. Kitajima, "A Novel Harmonic Current Control for IPMSMs," *The 2005 International Power Electronics Conference A Multi-Mode Charging Circuit for Rechargeable Batteries*, pp. 1569–1574, 2005.

(5) N. Nakao, K. Tobari, T. Sugino, Y. Ito, M. Mishima, and D. Maeda, "Torque ripple suppression control for PMSMs using feedforward compensation and online parameter estimation," *IEEJ Transactions on Industry Applications*, vol. 141, no. 1, pp. 18–27, 2021.

(6) H. Fujimoto, F. Kawakami, and S. Kondo, "Switching Based Repetitive Control for Hard Disk Drives : Experiments on RIDR and RPTC Methods," *Proceedings of the 2004 IEEE International Conference on Control Applications, 2004.*, vol. 1, no. 1, pp. 99–104, 2004.

(7) T. Nakai and H. Fujimoto, "Harmonic current suppression method of SPM motor based on repetitive perfect tracking control with speed variation," *IECON Proceedings (Industrial Electronics Conference)*, no. 2, pp. 1210–1215, 2008.

(8) H. Fujimoto, Y. Hori, and A. Kawamura, "Perfect tracking control based on multirate feedforward control with generalized sampling periods," *IEEE Transactions on Industrial Electronics*, vol. 48, no. 3, pp. 636–644, 2001.

(9) H. M. Flieh, R. D. Lorenz, E. Totoki, S. Yamaguchi, and Y. Nakamura, "Dynamic Loss Minimizing Control of a Permanent Magnet Servomotor Operating even at the Voltage Limit When Using Deadbeat-Direct Torque and Flux Control," *IEEE Transactions on Industry Applications*, vol. 55, no. 3, pp. 2710–2720, 2019.

(10) G. Bertotti, "General Properties of Power Losses in Soft Ferromagnetic Materials," *IEEE Transactions on Magnetics*, vol. 24, no. 1, pp. 621–630, 1987.

(11) K. Yamazaki and Y. Seto, "Iron Loss Analysis of Interior Permanent-Magnet Synchronous Motors — Variation of Main Loss Factors Due to Driving Condition," *IEEE Transactions on Industry Applications*, vol. 42, no. 4, pp. 1045–1052, 2006.

(12) H. Ge, B. Bilgin, and A. Emadi, "Global Loss Minimization Control of PMSM Considering Cross-Coupling and Saturation," *2015 IEEE Energy Conversion Congress and Exposition (ECCE)*, pp. 6139–6144, 2015.

(13) H. Zhang, M. Dou, and J. Deng, "Loss-minimization strategy of nonsinusoidal back EMF PMSM in multiple synchronous reference frames," *IEEE Transactions on Power Electronics*, vol. 35, no. 8, pp. 8335–8346, 2020.

(14) K. Nakamura, H. Fujimoto, and M. Fujitsuna, "Torque ripple suppression control for PM motor with current control based on PTC," *2010 International Power Electronics Conference - ECCE Asia -, IPEC 2010*, no. 1, pp. 1077–1082, 2010.

(15) A. Kawamura, H. Fujimoto, and T. Yokoyama, "Survey on the real time digital feedback control of PWM inverter and the extension to multi-rate sampling and FPGA based inverter control," *IECON Proceedings (Industrial Electronics Conference)*, no. 1, pp. 2044–2051, 2007.

(16) K. Sakata and H. Fujimoto, "Perfect tracking control of servo motor based on precise model with PWM hold and current loop," *Fourth Power Conversion Conference-NAGOYA, PCC-NAGOYA 2007 - Conference Proceedings*, pp. 1612–1617, 2007.

(17) T. Miyajima, H. Fujimoto, and M. Fujitsuna, "Control method for IPMSM based on PTC and PWM hold model in overmodulation range -Study on robustness and comparison with anti-windup control-," *2010 IEEE Energy Conversion Congress and Exposition, ECCE 2010 - Proceedings*, pp. 2844–2850, 2010.

(18) K. K. Chew and M. Tomizuka, "Digital Control of Repetitive Errors in Disk Drive Systems," *IEEE Control Systems Magazine*, vol. 10, no. 1, pp. 16–20, 1990.

(19) T. Nakai and H. Fujimoto, "Harmonic current suppression method of SPM motor based on repetitive perfect tracking control with speed variation," *IECON Proceedings (Industrial Electronics Conference)*, no. 2, pp. 1210–1215, 2008.

(20) S. Morimoto, M. Sanada, and Y. Takeda, "Wide-Speed Operation of Interior Permanent Magnet Synchronous Motors with High-Performance Current Regulator," *IEEE Transactions on Industry Applications*, vol. 30, no. 4, pp. 920–926, 1994.

(21) H. Iwata, K. Ohishi, Y. Yokokura, Y. Okada, Y. Ide, D. Kuraishi, and A. Takahashi, "Robust Estimation Method for Stator Temperature Based on Voltage Disturbance Observer Autotuning Resistance for SPMSM," *IEEJ Journal of Industry Applications*, vol. 9, no. 4, pp. 341–350, 2020.